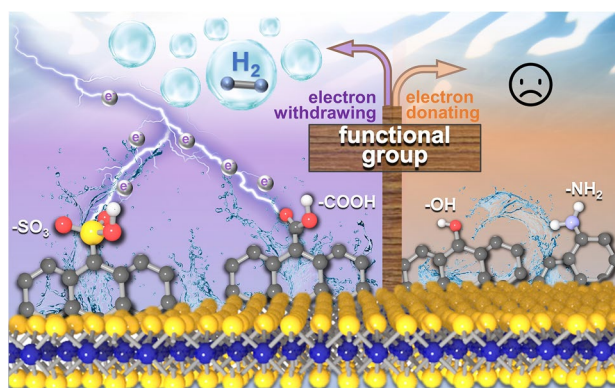# Graphene Quantum Dot-Mediated Atom-Layer Semiconductor Electrocatalyst for Hydrogen Evolution

Bingjie Hu[1], Kai Huang[2], Bijun Tang[3], Zhendong Lei[3] ✉, Zeming Wang[1], Huazhang Guo[1], Cheng Lian[2] ✉, Zheng Liu[3] ✉, Liang Wang[1,3] ✉

HIGHLIGHTS

- The functional groups on graphene quantum dots (GQDs) for boosting the formation of MoS_2 nanosheets via theoretical calculations were predicted.

- Near atom-layer-QD@SO_3 with about 2 nm were synthesized using a functionalized GQD-induced in-situ bottom-up approach.

- Mechanistic insight on the role of functionalized GQDs was elaborated, namely, electron-withdrawing group functionalized GQDs facilitate the formation of nanosheet architectures of MoS_2 compared to electron-donating group.

ABSTRACT The hydrogen evolution reaction performance of semiconducting 2H-phase molybdenum disulfide (2H-MoS_2) presents a significant hurdle in realizing its full potential applications. Here, we utilize theoretical calculations to predict possible functionalized graphene quantum dots (GQDs), which can enhance HER activity of bulk MoS_2. Subsequently, we design a functionalized GQD-induced in-situ bottom-up strategy to fabricate near atom-layer 2H-MoS_2 nanosheets mediated with GQDs (ALQD) by modulating the concentration of electron withdrawing/donating functional groups. Experimental results reveal that the introduction of a series of functionalized GQDs during the synthesis of ALQD plays a crucial role. Notably, the higher the

concentration and strength of electron-withdrawing functional groups on GQDs, the thinner and more active the resulting ALQD are. Remarkably, the synthesized near atom-layer ALQD-SO_3 demonstrate significantly improved HER performance. Our GQD-induced strategy provides a simple and efficient approach for expanding the catalytic application of MoS_2. Furthermore, it holds substantial potential for developing nanosheets in other transition-metal dichalcogenide materials.

KEYWORDS Graphene quantum dots; MoS_2 nanosheets; Atom-layer; Semiconductor electrocatalysts; Hydrogen evolution reaction

Bingjie Hu and Kai Huang have contributed equally to this work.

✉ Zhendong Lei, zhendong.lei@ntu.edu.sg; Cheng Lian, liancheng@ecust.edu.cn; Zheng Liu, z.Liu@ntu.edu.sg; Liang Wang, wangl@shu.edu.cn

[1] Institute of Nanochemistry and Nanobiology, School of Environmental and Chemical Engineering, Shanghai University, 99 Shangda Road, BaoShan District, Shanghai 200444, People's Republic of China

[2] State Key Laboratory of Chemical Engineering, Shanghai Engineering Research Center of Hierarchical Nanomaterials, School of Chemistry and Molecular Engineering, East China University of Science and Technology, Shanghai 200237, People's Republic of China

[3] School of Materials Science and Engineering, Nanyang Technological University, 50 Nanyang Avenue, Singapore 639798, Singapore

1 Introduction

The electrocatalytic production of hydrogen from water represents a promising approach for achieving global carbon neutrality through the utilization of clean energy sources [1–4]. To enable efficient energy conversion, robust and cost-effective electrocatalysts are necessary [4, 5]. Semiconducting 2H-phase molybdenum disulfide (2H-MoS$_2$), the most extensively studied transition metal dichalcogenides, has emerged as a leading contender for replacing commercial Pt-based catalysts due to its low cost, earth abundance, and non-toxicity [6, 7]. Unlike bulk MoS$_2$, near single-layer 2H-MoS$_2$ nanosheets (2H-MoS$_2$ NSs) have garnered significant attention due to their high specific surface area and surface activity, rendering them attractive candidates for catalytic hydrogen evolution reaction (HER), electronics, and batteries [8–10]. Nevertheless, the HER capacities of 2H-MoS$_2$ NSs are currently limited. Several chemical or physical approaches have been explored to mediate the electronic structure of 2H-MoS$_2$ NSs, including light irradiation, energetic ion bombardment, laser ablation, and physical sputtering [4, 6, 11]. However, these methods usually require harsh experimental conditions, such as supercritical hydrothermal, explosive gas atmosphere, and high-risk reagents [12–15], posing risks and limiting practical applications. Therefore, there is a pressing need to develop a method for producing near atom-layer 2H-MoS$_2$ under mild conditions to reveal their properties and electrocatalysis applications.

Recently, 2H-MoS$_2$ NSs were synthesized using hydrothermal or solvothermal methods. However, their electrocatalytic performance remains suboptimal due to intrinsic poor electronic conductivity. To address this issue, incorporating carbon materials with 2H-MoS$_2$ NSs has been explored as an effective strategy to enhance their conductivity [16, 17]. However, the combination of 2H-MoS$_2$ NSs with carbon materials leads to irreversible aggregation caused by van der Waals attractions between the sheets. This aggregation reduces the number of exposed active sites, resulting in a decrease in electrocatalytic activity [18]. Graphene quantum dots (GQDs), a novel type of carbon nanomaterials, has attracted significant attention for their unique characteristics, including tunable size, sufficient active sites, and abundant surface functional groups. These features make them highly promising for

applications in the electrocatalysis industry [16, 17]. In our previous studies, we successfully utilized GQDs as inducers of a 2D structure and inhibitors of stacking to facilitate the formation of metal–organic framework (MOF) NSs [18]. This was achieved through a one-step room-temperature "bottom-up" synthesis strategy, eliminating the need for complex and low-yield exfoliation processes. GQDs possess a large specific surface energy and small size, which effectively prevent outgrowth agglomeration and promote the formation of NSs. Additionally, the introduction of carboxylated GQDs boosts the electrocatalytic performance of MOF NSs.

Inspired by previous work, herein, we report a facile *in-situ* GQDs-assisted hydrothermal method to synthesize near atom-layer 2H-MoS$_2$ NSs (ALQD). A series of GQDs with different functional groups have been designed and fabricated [19–21]. Various techniques have been conducted to unravel the morphology, composition, and structure of as-prepared ALQD, including scanning transmission electron microscopy (TEM), atomic force microscope (AFM), X-ray photoelectron spectroscopy (XPS), Raman spectroscopy, and X-ray diffraction (XRD). The successful synthesis of the ALQD is attributed to the introduction of GQDs, which simultaneously enlarge the layer space and lower the formation energy of ALQD, guided by our theoretical calculations. As a proof-of-concept application, the hydrothermal-grown ALQD demonstrate superior HER performance compared to bulk MoS$_2$ and pristine 2H-MoS$_2$ NSs. Our study provides a landmark hint in the development of atom-layer semiconductor electrocatalysts for hydrogen production from water.

2 Experimental Section

2.1 Synthesis of SO$_3$-GQDs

We obtained SO$_3$-GQDs by a simple one-step method, based on the hydrothermal molecular fusion route. Yellow 1,3,6-trinitropyridine (0.5 g) and Na$_2$SO$_3$ (0.5 g) were dispersed in 50 mL deionized water and stirred for 0.5 h. The suspension was transferred to a 100-mL autoclave Teflon-lined stainless-steel autoclave and heated at 180 °C for 12 h. After cooling to room temperature, the clear solution obtained by filtration was dialyzed with a

dialysis bag for three days to remove unreacted sodium salt, and dried at 60 °C. The synthesis process of other SO_3-GQDs is similar to that of the process, except the added different sulfonic precursors: 4-hydrazinobenzenesulfonic acid for SO_3-GQDs-1, 4-hydroxybenzenesulfonic acid for SO_3-GQDs-2, and 1-amino-2-naphthol-4-sulfonic acid for SO_3-GQDs-3.

2.2 Synthesis of NH$_2$-GQDs

Imitating the synthesis process of SO_3-GQDs, we replaced the sulfonic acid source with equal mass $NH_3·H_2O$ and got NH_2-CQDs.

2.3 Synthesis of OH-GQDs

Imitating the synthesis process of SO_3-GQDs, we replaced the sulfonic acid source with NaOH, then the obtained powder named O-GQDs solved in the mixture of DMF and pure water in the ratio of five to one, and transferred into a 100-mL autoclave Teflon-lined stainless-steel autoclave and heated at 200 °C for 10 h. Finally, the OH-CQDs were gained.

2.4 Synthesis of COOH-GQDs

The O-GQDs powder is completely dissolved in water, then sulfuric acid is dripped into the solution until pH = 2~3. The acidulated solution hydrothermal was transferred to a 100-mL autoclave Teflon-lined stainless-steel autoclave and heated at 180 °C for 10 h to obtain COOH-GQDs.

2.5 Preparation of Bulk MoS$_2$ and ALQD

Typically, 1.235 g $(NH_4)_6Mo_7O_{24}·4H_2O$ (1 mmol), 2.28 g thiourea (30 mmol) and 0.1 g SO_3-GQDs powder is dissolved in 40 mL distilled water. The suspension was stirred for 1 h to form a homogeneous solution. The solution was transferred to a 100-mL Teflon-lined stainless-steel autoclave and heated at 200 °C for 20 h. After naturally cooled to room temperature, the product was collected by centrifugation and washed with ethanol. The purified black ALQD-SO_3 was dried at 60 °C for structural characterization and property measurement. The other products (ALQD-SO_3-1, ALQD-SO_3-2, ALQD-SO_3-3, ALQD-COOH, ALQD-OH, ALQD-NH$_2$) are obtained by an analogical routine, replacing SO_3-GQDs with corresponding GQDs. The synthesis process of bulk MoS_2 is similar to that of the process, except the exclusion of SO_3-GQDs.

2.6 Electrochemical Measurements

All the electrochemical measurements were performed in a three-electrode system on an electrochemical work-station (CHI760e, Shanghai Chenhua Instruments Co., China) at room temperature. All tests above without iR-compensation. The electrocatalyst (5.0 mg) was dissolved in the mixture of 700 μL deionized water, 250 μL isopropyl alcohol, and 50 μL 5% Nafion solution, and then the electrocatalytic ink for all electrochemical tests was obtained. More importantly, the catalyst ink should be ultrasonically treated in an ice bath for 1 h to be fully mixed. Then, the aqueous dispersion of the catalyst (10 μL, 5.0 mg mL^{-1}) was completely dropped to the glassy carbon electrode. We applied a rotating disk electrode (RDE) to proceed HER performance testing in a three-electrode cell configuration. A saturated Hg/Hg_2Cl_2 electrode (acid electrolyte) as the reference electrode, a graphite rod as the counter electrode, and the glassy carbon electrode supported catalysts as the working electrode. All potentials were calibrated to the RHE by the following equation:

$$E_{RHE} = E\left(Hg/Hg_2Cl_2\right) + 0.059\,pH + 0.244 \qquad (1)$$

The HER performance was measured in N_2 saturated aqueous 0.5 M H_2SO_4 (pH = 0.3) at a scan rate of 50 mV s^{-1} with 100 cyclic voltammetry (CV) cycles in the range of 0.3 to −0.8 V RHE. Linear sweep voltammetry (LSV) with a scan rate of 10 mV s^{-1} at 1600 rpm after 100 CV cycles in the range of 0.3 to −0.8 V RHE. Tafel curves were then obtained from linear sweep voltammograms using a scan rate of 10 mV s^{-1}. The electrochemical impedance spectroscopy (EIS) was executed in the frequency range of 100 kHz to 1 mHz with a modulation amplitude of 10 mV.

Cycling stability tests. The LSV curves were recorded for the first cycle and after 1000 CV sweeps between 0.3 and −0.8 V RHE at 50 mV s^{-1}. All the LSV curves were performed in the different electrolytes at a scan rate of 10 mV s^{-1}.

Durability measurements. The chronoamperometry test of catalysts runs for no less than 20 h under the condition of constant overpotential at 245 mV, corresponding to current density of 10 mA cm^{-2} (η10).

2.7 Material Characterization

Transmission electron microscopy (TEM) measurements were performed on a JEOL JEM-2100F electron microscope operating at 200 kV. The atomic force microscope (AFM) images were characterized using Bruker Dimension Icon AFM. The crystal phase structures of samples were investigated through X-ray diffraction, with a nickel-filtered Cu-Kα radiation source (XRD: Rigaku D/max-2500, Japan). The functional groups on the sample surface were measured by X-ray photoelectron spectroscopy (XPS, Thermo Fischer, ESCALAB250Xi). Raman spectra were assessed using Cora 5001 (Anton Paar OptoTec GmbH), which was implemented utilizing 785 nm as the excitation light source. Fourier transform infrared (FTIR) spectra were measuremed on a Nicolet iS50 spectrometer (Thermofisher) with a resolution of 0.09 cm^{-1} and a DLaTGS detector within the range 4000–400 cm^{-1}. The temperature-programmed de-sorption (TPD) tests were conducted utilizing a Micromeritics Anton-Paar ChemBET characterization system with a quartz U-tube reactor and detected using a TCD. The electron conductivity of samples was characterized by a four-probe powder resistivity tester (Suzhou Jingge Electronic Co., Ltd. ST2722). The contact angle measurements are typically done by using Theta Flow equipment (Biolin Scientific) with optical and force tensiometers to perform calculations.

2.8 Computational Details

The DFT calculations were implemented in the Vienna ab initio Simulation Package (VASP) [22]. The Perdew-Burke-Ernzerhof (PBE) method was adopted to establish the exchange correlation functional [23]. The energy cutoff was set to 500 eV and the Gaussian smearing was used (SIGMA = 0.05 eV). For all configuration, 2 × 3 × 4 Gamma K-point grid was constructed by vaspkit. In the calculation process, the dispersion interaction was corrected by DFT-D2 method [24]. The DFT calculations were considered to be convergent when the forces and the energy less than 0.02 eV Å^{-1} and 10^{-5} eV atom^{-1}, respectively. For the Gibbs

free energy calculations of HER process, the computational hydrogen electrode (CHE) method proposed by Nørskov was used [25]. The Gibbs free energy is given by Eq. (2):

$$G = E + E_{ZPE} + \int C_{p}dT - TS \tag{2}$$

where E and E_{ZPE} are the total energy of system and the zero-point energy, respectively. C_{p} is the heat capacity; T is the temperature (298.15 K), and S is the entropy. The configuration of 2H-MoS$_2$ was exported from Materials Project, and a 10 × 4 × 1 supercell was constructed in our DFT calculations. The GQDs consist of 102 C atoms, the edge is saturated by adding H atom. The size of GQDs was 1.36 × 2.17 nm. The functionalized GQDs were constructed by replacing one H atoms with the functional group. The small (0.51 × 0.94 nm) and medium sizes (0.94 × 1.93 nm) of GQDs consist of 84 and 27 C atoms, respectively. For the calculations of layer spacing, the lattice parameters were relaxed during the DFT calculations. For the Gibbs free energy calculations, the lattice parameters were fixed.

The MD simulations were implemented by Forcite module in Materials Studio. The universal forcefield was selected for the MD simulation. The Ewald method was used to handle the long-range electrostatic interactions with a cutoff radius of 1.2 nm [26]. The atom-based summation method was employed to treat the van der Waals interaction with a cutoff radius of 1.8 nm. The Nose thermostat was selected to control the temperature for dynamics simulation [27]. The time step is set as 2 fs for all the simulations. The structures of GQDs vertical/parallel insertion 2H-MoS$_2$ were considered in 6.42 × 5.11 × 2.13 nm (vertical) and 6.42 × 5.11 × 0.99 nm (parallel). The total atom number of 1483 for two systems. The layer spacings of 2H-MoS$_2$ were obtained by DFT calculations. All systems were first exposed to energy minimization by steepest descent method. Then, the systems were equilibrated for 5 ns in NPT ensemble. After that, production MD runs were performed for 15 ns in the NPT ensemble.

3 Results and Discussion

3.1 Theoretical Prediction of the Optimum Structure of ALQD-SO$_3$

The bulk MoS$_2$ is generally obtained by the direct hydrothermal fabrication, which exhibits the inadequate HER performance. Building upon the success in preparing MOF NSs through the introduction of GQDs in the synthesis

procedure, we employed theoretical calculations to predict the structures and formation energies of four types of ALQD. Furthermore, molecular dynamics (MD) simulation confirmed the structural stability of GQDs in 2H-MoS$_2$. As schematically illustrated in Fig. 1a, the energy of GQDs with vertical insertion in 2H-MoS$_2$ is lower than that of GQDs with parallel insertion ($\Delta E = 371$ eV), indicating that the former is the more stable structure model. The MD results were used to establish the structures of ALQD for density functional theory (DFT) calculation, which are depicted in Fig. 1b.

The layer spacing of 2H-MoS$_2$ upon introduction of GQDs was first investigated. As shown in Fig. 1c, the layer spacing (d) of 2H-MoS$_2$ increases upon the introduction of

electron-withdrawing group functionalized GQDs, which is larger than that of electron-donating group functionalized GQDs. Specifically, ALQD-SO$_3$ exhibits the largest layer spacing of 21.28 Å, while ALQD-OH presents the smallest layer spacing of 19.89 Å. These findings agree well with prior research [18], which demonstrate that increased layer spacing can prevent NS stacking. The calculation results further reveal that the introduction of GQDs-SO$_3$ in 2H-MoS$_2$ can effectively inhibit stacking and promote the formation of 2D 2H-MoS$_2$ NSs. Additionally, the formation energies of the four different types of ALQD were calculated, providing further evidence for the observed differences in layer spacing. Introducing electron-withdrawing group functionalized GQDs into 2H-MoS$_2$ NSs requires more energy to expand
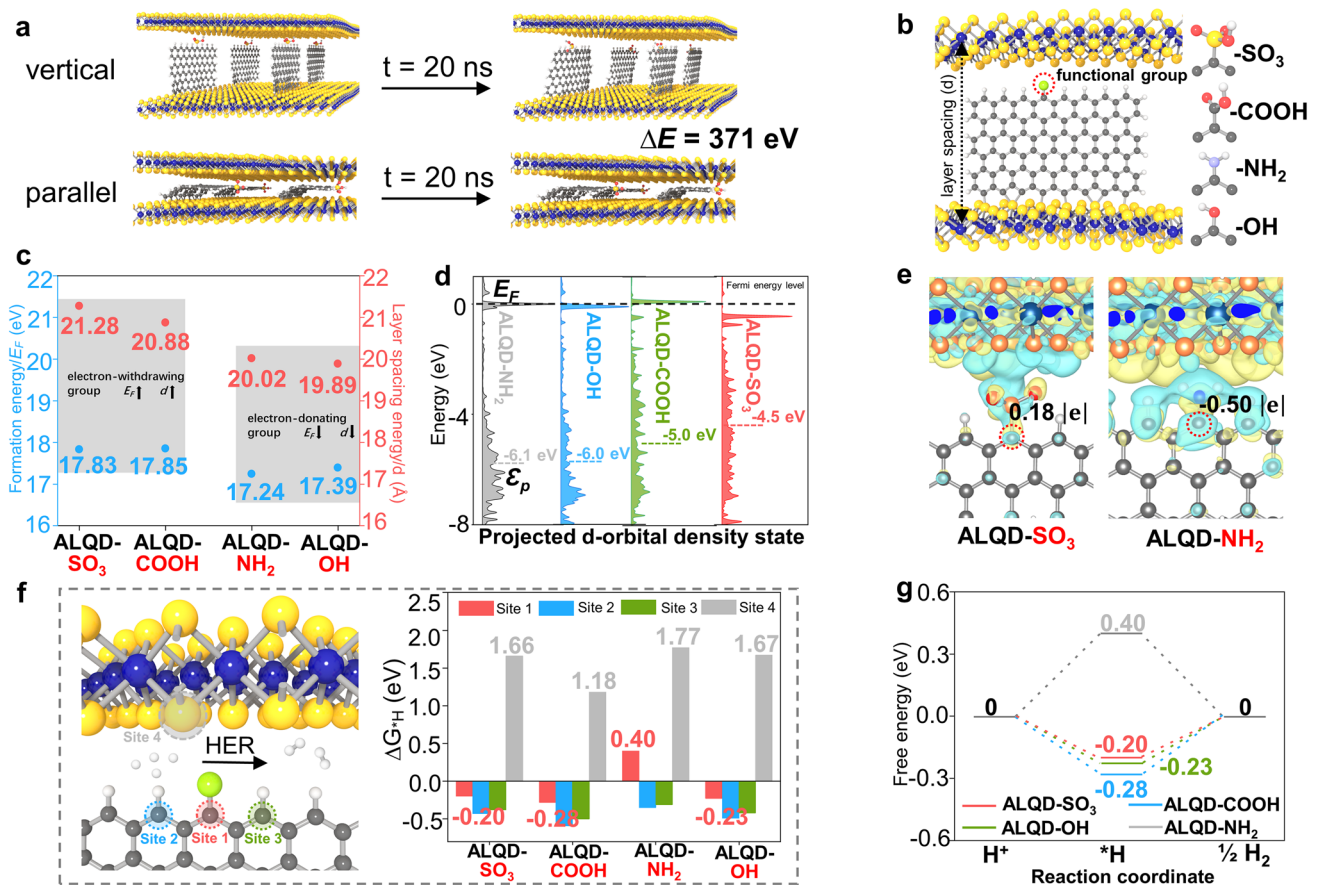
Fig. 1 Structures, charge properties and HER performance of materials by theoretical prediction. **a** Structure stability of GQDs into the 2H-MoS$_2$. **b** Structures of four types of ALQD, d is the layer spacing of 2H-MoS$_2$ NSs by measuring the vertical distance of two Mo atoms. The yellow, blue, grey, white, and green ball represent S, Mo, C, H, and functional group, respectively. **c** Layer spacing and formation energy of four types of ALQD. **d** PDOS and p-band center of C atom connected to the -SO$_3$ and -NH$_2$. **e** Difference charge density and Bader charge of C atom connected to the -SO$_3$ and -NH$_2$. The green and red isosurface denote the decrease and increase in electron density, respectively, and the value is $\pm 3 \times 10^{-4}$ e Bohr^{-3}. **f** Gibbs free energy change (ΔG_{*H}) of HER process on four sites of four types of ALQD. **g** Gibbs free energy profile of HER process for the C sites connected to the functional groups on four types of ALQD

the layer spacing compared to the introduction of electron-donating group functionalized GQDs, as evidenced by the higher formation energy of ALQD-SO$_3$/COOH compared to ALQD-NH$_2$/OH (0.44–0.65 eV).

The introduction of functionalized GQDs in 2H-MoS$_2$ NSs affects not only the layer spacing, but also the electronic structure of ALQD, leading to improved electrocatalytic performance. The partial density of states (PDOS) and p-band center (ε_p) of the C site directly linked to the functional group (C-SO$_3$ and C-NH$_2$) on GQDs were evaluated, as shown in Fig. 1d. The ε_p value of the active site close to the Fermi energy level is crucial for strong adsorption for intermediates [28, 29]. The results demonstrate that the ε_p value of C-SO$_3$ (-4.5 eV) is closer to the Fermi energy level than that of C-NH$_2$ (-6.1 eV). Notably, the ε_p value of C-COOH is 1.0 eV lower than that of C–OH (Fig. S1). The data of p-band center indicate that 2H-MoS$_2$ NSs introduced by electron-withdrawing group functionalized GQDs possess enhanced adsorption capacity for intermediates and exhibit superior electrocatalytic performance. The Bader charge analysis also reveals strong electron transfer between the C atom and functional group (Fig. 1e). The C atom linked to the -SO$_3$ functional group obtains 0.18 |e|, while the C-NH$_2$ loses 0.50 |e|. Similar behavior is observed for C-COOH and C–OH (Fig. S1). Increased electrons at the active sites (C-SO$_3$/COOH) can enhance the electrocatalytic performance, such as HER. In addition, the change of the charge distribution on the surface of 2H-MoS$_2$ NSs through the functional group of GQDs are evident from the difference charge density, indicating that 2H-MoS$_2$ NSs can be activated by electron-withdrawing groups on GQDs.

Considering the electrocatalytic performance of materials is strongly affected by their structure and electronic properties, the Gibbs free energy change (ΔG_{*H}) of the HER process was calculated for four kinds of ALQD in Figs. 1f and S2-S5. Four different sites on the ALQD were considered: C site connected to the functional group (site 1), two C sites near the functional group (site 2, 3) and S site (site 4). The C sites connected to the functional group are found to be the active sites for the HER process, except for ALQD-NH$_2$ (Fig. 1f). The Bader charges of C atoms near -NH$_2$ (0.08 |e| and -0.01 |e|) are more positive than those of C atoms connected to -NH$_2$ (-0.50 |e|), suggesting that C atoms near -NH$_2$ are the active sites for the HER process (Fig. S6). In addition, the S site of the ALQD-COOH exhibits superior HER performance compared to other ALQD, indicating that

the electron-withdrawing -COOH group can activate the S sites of 2H-MoS$_2$.

Figure 1g presents the Gibbs free energy profile of the HER process for the C sites connected to the functional group. ALQD-SO$_3$ exhibits superior HER performance because of its lowest ΔG_{*H} value of -0.20 eV, while ALQD-NH$_2$ shows poor HER performance. Interestingly, ALQD-OH performs better in the HER process compared to ALQD-COOH, despite the relatively small differences in their ΔG_{*H} values (0.03–0.08 eV). This should be attributed to the potential impact of the size of GQDs on the regulation effect of functional groups. To evidence this hypothesis, the ΔG_{*H} values for different-sized ALQD (small size: 0.51×0.94 nm; medium size: 0.94×1.93 nm) were calculated (Figs. S7 and S8). The trend is observed for the medium-sized ALQD: ΔG_{*H} increases from electron-withdrawing group functionalized ALQD to electron-donating group functionalized ALQD. However, there is a significant difference in the ΔG_{*H} values of the four types of small-sized ALQD. Specifically, ALQD-SO$_3$ and ALQD-NH$_2$ show the minimum (-0.18 eV) and maximum (0.48 eV) ΔG_{*H} values, respectively. Based on these results, ALQD-SO$_3$ should be the most promising one to display optimal HER performance among the four types of ALQD.

3.2 Morphological and Structural Characterization of ALQD-SO$_3$

As schematically shown in Fig. 2, our *in-situ* synthesis strategy is based on a one-pot hydrothermal method that utilizes SO$_3$-GQDs in the synthesis process to tune the thickness of the 2H-MoS$_2$. We have achieved possible industrial preparation and obtained a large number of samples by one-time preparation, producing approximately about 1.3 g, with a production yield of 35.96% (Fig. S9). The unbound SO$_3$-GQDs on the sample surface can be simply removed by the centrifugal cleaning by DI water, owing to the super-hydrophilic characteristics of SO$_3$-GQDs [19]. A series of morphological and structural characterizations have been performed to investigate the 2D structure formation and conversion of ALQD-SO$_3$. The TEM image of ALQD-SO$_3$ shows a sheet structure (Fig. 2a), with SO$_3$-GQDs uniformly attached to the surface of the ultrathin 2H-MoS$_2$ NSs. The AFM image shown in Fig. 2c further reveals its uniform thickness with
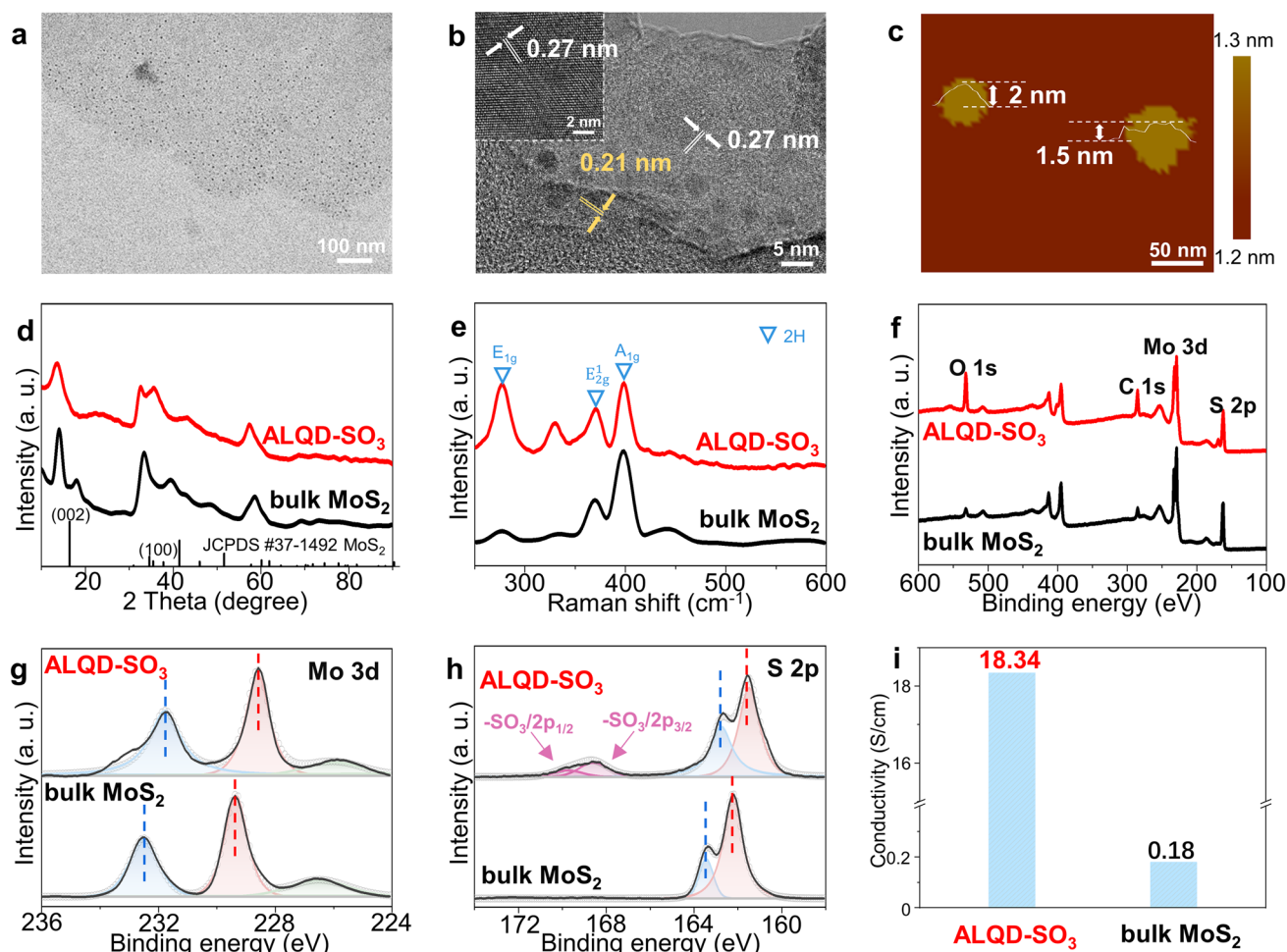
Fig. 2 Morphological and structural characterization of synthesized materials. **a** TEM image of ALQD-SO$_3$. **b** High-resolution TEM image of ALQD-SO$_3$. The inset in **b** shows the regular lattice of zoomed-in MoS$_2$ NSs. **c** AFM image of ALQD-SO$_3$. **d** XRD patterns of ALQD-SO$_3$ and bulk MoS$_2$. **e** Raman spectra of ALQD-SO$_3$ and bulk MoS$_2$. **f** XPS survey, and high-resolution XPS **g** Mo 3d and **h** S 2p spectra of ALQD-SO$_3$ and bulk MoS$_2$. **i** Electrical conductivities of ALQD-SO$_3$ and bulk MoS$_2$

an average height of about 2 nm, further supporting the NS architecture of the as-prepared ALQD-SO$_3$. Conversely, the bulk MoS$_2$ exhibits an aggregation appearance, with a height as high as 120 nm, far away from the NS morphology (Figs. S10 and S11). The high-resolution TEM image (Fig. 2b) shows a lattice fringe of 0.27 nm attributed to the (100) plane of 2H-MoS$_2$ [30]. Apart from the observed lattice of the primary NSs, a distinct lattice fringe of the introduced SO$_3$-GQDs (0.21 nm) was found [31], which indicates that SO$_3$-GQDs were successfully coupled to the 2H-MoS$_2$ substrates. The high quality of the as-synthesized samples demonstrates the superiority of the GQD-induced facile hydrothermal synthesis method [12].

As shown in the XRD pattern (Fig. 2d), the peak position of bulk MoS$_2$ prepared by our one-pot hydrothermal method without SO$_3$-GQDs perfectly matches the standard pattern of 2H-MoS$_2$. The strongest peak is noticeable around 14° wide (002) peak, which is attributed to the interplanar spacing (6.15 Å) [32]. The interplanar spacing (2.7 Å) of the (100) peak located at 2θ≈32° [33], is consistent with high-resolution TEM image. However, the (002) peak intensity of as-prepared samples through SO$_3$-GQDs regulation is dramatically weakened, demonstrating a few-layer graphene-like stacked structure [34]. Furthermore, the strongest diffraction peak of ALQD-SO$_3$ exhibits a blue-shift compared to that of bulk MoS$_2$, suggesting an increased interlayer distance in ALQD-SO$_3$ [35]. This serves as crucial evidence for the

formation of NS architectures caused by the opening interlayer spacing of SO$_3$-GQDs. The structures of bulk MoS$_2$ and ALQD-SO$_3$ are further analyzed by their Raman spectra (Fig. 2e), which exhibit two characteristic peaks of 2H-MoS$_2$ at 376 and 398 cm^{-1}, originating from the in-plane stretching and out-of-plane vibration Raman modes of S–Mo–S, respectively [36, 37]. The extra peaks demonstrate that the presence of GQDs in ALQD induced structural configuration changes leads to a distorted 2H phase in the basal plane of MoS$_2$, thereby revealing the coordination of MoS$_2$ with GQDs on the ALQD nanosheets [38].

The chemical nature and stoichiometric compositions of as-prepared samples via SO$_3$-GQDs-regulation were confirmed by XPS (Fig. 2f–h). The deconvoluted S 2p spectrum of ALQD-SO$_3$ contains the peak at $\approx$168 eV corresponding to SO$_3$ configurations, implying the presence of SO$_3$-GQDs [18]. The deconvoluted Mo 3d peaks possess two peaks at 229.4 and 232.2 eV, corresponding to Mo^{4+} 3$d_{5/2}$ and 3$d_{3/2}$ of the 2H phase, respectively, confirming the 2H phase of bulk MoS$_2$ [39, 40]. Additionally, a blueshift of $\approx$0.8 eV to lower binding energy (228.6 and 231.8 eV) is observed in ALQD-SO$_3$. This shift phenomenon can be ascribed to the introduction of electron-withdrawing group functionalized SO$_3$-GQDs, leading to the increase in the electron density around the Mo and S sites, consistent with the result of our theoretical prediction (Fig. S3) [41, 42]. According to the stoichiometry analysis result (Table S1), the Mo:S molar ratio decreases significantly from about 1:1.59 to 1:1.35 after SO$_3$-GQDs-regulation. The storage stability of the synthesized samples was further investigated by XPS measurement. As shown in Fig. S12, the spectra of ALQD-SO$_3$ produced 6 months ago and freshly produced exhibit no significant difference, demonstrating the excellent storage stability of our designed materials.

Notably, the electrical conductivity of ALQD-SO$_3$ is two orders of magnitude higher than that of bulk MoS$_2$ (18.34 vs 0.18 S cm^{-1}), which is beneficial for the charge transfer kinetics in HER process (Fig. 2i) [43]. In electrocatalyst applications, the hydrophilic property increases the interfacial contact area between the catalyst surface and aqueous electrolyte, thereby improving the overall catalytic performance [44]. Unignored, the higher hydrophilicity of ALQD-SO$_3$ than that of bulk MoS$_2$ further verifies the introduction of the electron-withdrawing group functionalized SO$_3$-GQDs can enhance the electrocatalysis activities of the designed ALQD-SO$_3$ (Fig. S13). In light of these analyses,

the results corroborate the more efficient HER application of semiconducting ALQD-SO$_3$ [45, 46].

3.3 Evaluation Toward Electrochemical Hydrogen Evolution

To evaluate the influence of SO$_3$-GQDs on HER performance, the electrochemical characteristics of various MoS$_2$ samples were measured using a rotating disk electrode (RDE) at a rate of 1600 rpm in 0.5 M H$_2$SO$_4$ (see the Materials and Methods section for details). Linear sweep voltammetry (LSV) curves are exhibited in Fig. 3a. The overpotentials (η) at a current density of 10 mA cm^{-2} of ALQD-SO$_3$ NSs is 1.85 times lower than bulk MoS$_2$ (245 and 453 mV vs RHE), which is consistent with the theoretical calculations of ΔG_{*H} = -0.20 eV. Moreover, we synthesized a sample using the equal mass carbon black (CB) instead of SO$_3$-GQDs in the material synthesis procedure, and the as-synthesized sample exhibited poor HER activity similar to that of bulk MoS$_2$, implying that the regulation of the SO$_3$-functional group of GQDs plays the pivotal role in facilitating the HER capacities of MoS$_2$. To investigate the kinetic metrics, the Tafel slope is used to determine the rate-determining step for HER. From the extrapolation of the linear region of overpotential (η) versus log$j$ (Fig. 3b), we obtained Tafel slopes of 93.2 and 216.4 mV per decade for ALQD-SO$_3$ and bulk MoS$_2$, respectively. These results suggest that the role of GQDs in regulating MoS$_2$ electron is essential for improving the catalytic performance of HER. Both theoretical and experimental findings support the conclusion that ALQD-SO$_3$ exhibit superior HER catalytic activity and more effective active sites due to their unique structural characteristics.

To evaluate the effective electrochemical active surface areas (ECSAs) of the as-prepared electrocatalytic materials, cyclic voltammograms (CV) at different scan rates, and double-layer capacitances (C$_{dl}$) were measure. Figure 3c illustrates that the highest value of ECSA is observed for ALQD-SO$_3$, which correlated with its superior HER performance. The ECSA value of ALQD-SO$_3$ (10.2 mF cm^{-2}) is about three orders of magnitude higher than that of bulk MoS$_2$ (0.0835 mF cm^{-2}), indicating that the introduction of SO$_3$-GQDs in MoS$_2$ can significantly increase the ECSAs and expose more active sites for the electrochemical catalytic reaction. TPD measurements using NH$_3$ as a probe molecule
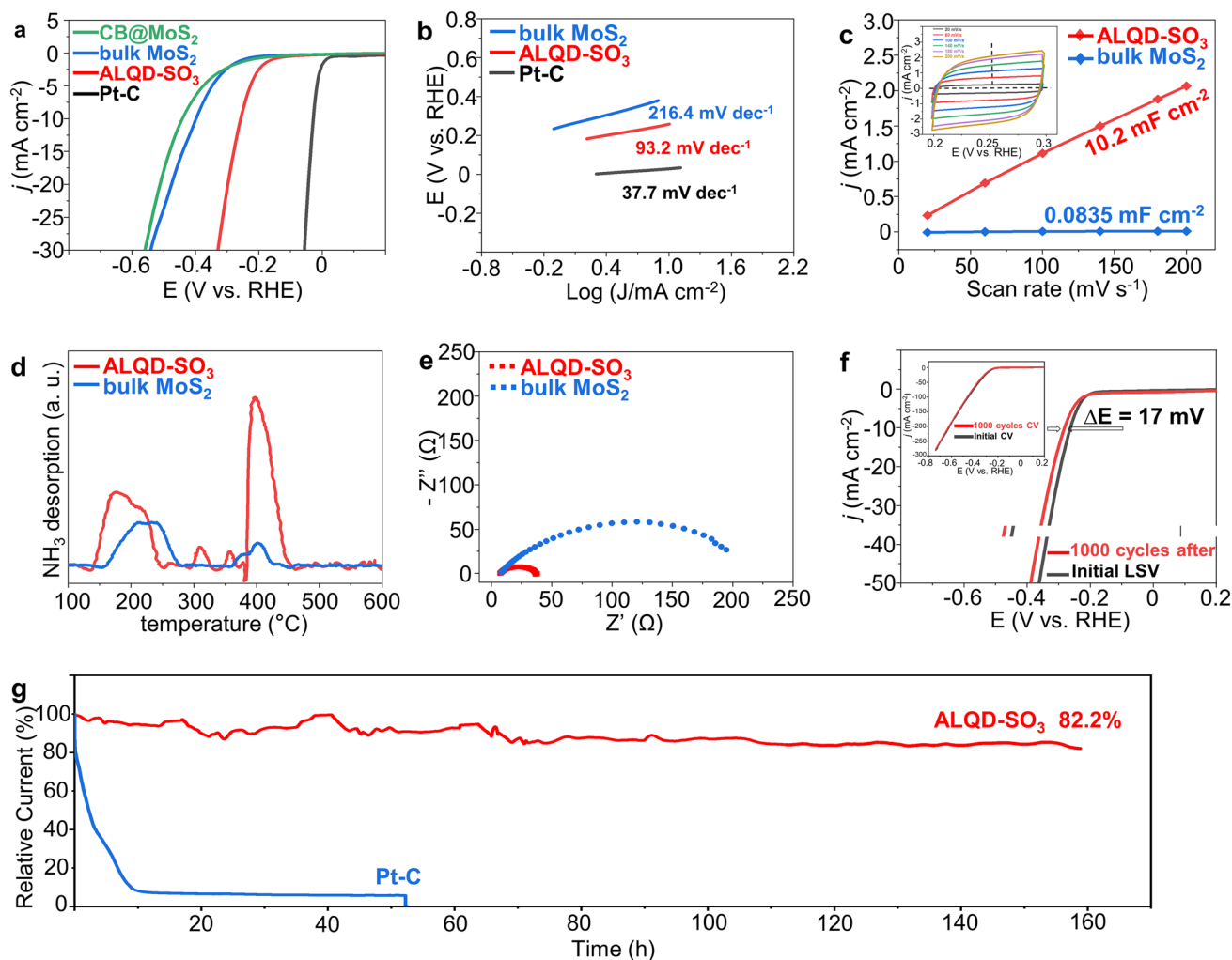
Fig. 3 HER performance of synthesized materials. **a** LSV curves of CB@MoS$_2$, bulk MoS$_2$, ALQD-SO$_3$ and PtC were performed in 0.5 M H$_2$SO$_4$ electrolyte. **b** The corresponding Tafel slopes were derived from LSV curves. **c** The ratio of the capacitive currents measured at 0.25 V vs RHE for bulk MoS$_2$ and ALQD-SO$_3$.The inset in **c** shows cyclic voltammograms of ALQD-SO$_3$ at a scan rate from 20 to 200 mV s^{-1}. **d** NH$_3$-TPD profiles of bulk MoS$_2$ and ALQD-SO$_3$. **e** Nyquist plots of bulk MoS$_2$ and ALQD-SO$_3$. **f** LSV curves measured before and after 1000 cycles at 0.2 to -0.8 V versus RHE. **g** Time dependence of current density at 250 mV versus RHE

were performed to further determine the type of active sites of the catalyst [38]. Figure 3d shows that bulk MoS$_2$ exhibits a weak Lewis acidic site to the NH$_3$ adsorption sites at 230 and 400 °C. However, the ALQD-SO$_3$ exhibits strong Lewis acidic sites to the NH$_3$ adsorption site at the above temperature due to its distinctive structure. Furthermore, there are two novel NH$_3$ adsorption sites at 310 and 360 °C owing to the addition of SO$_3$-GQDs. It is widely accepted that high-acidity sites such as -SO$_3$H groups of GQDs are the key to promoting HER activity. The Nyquist diagram in Fig. 3e shows that the charge transfer resistance (R$_{ct}$) of 2H MoS$_2$ (230 ω) is six times larger than that of ALQD-SO$_3$

(36 ω), indicating that appropriate SO$_3$-GQDs can accelerate interfacial electron transfer kinetics and charge transfer capacity to optimize HER activity [47, 48]. These results demonstrate the significantly improved intrinsic properties of ALQD-SO$_3$, providing a favorable platform for electrocatalytic activities.

In addition to the remarkable improvement of HER performance, we also evaluated their long-term cycling stability by conducting the CV process for 1000 cycles [49]. As depicted in Fig. 3f, the LSV curve of ALQD-SO$_3$ after 1000 cycles is very close to the initial one, demonstrating its remarkable stability as an HER electrocatalyst. The inset shows the CV

profiles of the first and 1000th cycles, revealing no visible degradation. Moreover, the catalytic stability of ALQD-SO$_3$ was studied by chronoamperometry (*i–t*), where the voltage was fixed at 0.25 V (vs RHE). Compared with Pt/C, ALQD-SO$_3$ exhibit greater durability and a higher current retention rate (82.2%) after 160 h of continuous operation (Fig. 3g). Such outstanding long-term catalytic stability suggests that our ALQD-SO$_3$ can serve as a high-efficiency HER electrocatalyst for large-scale practical applications.

To further confirm that the enhanced HER activity originates from the –SO$_3$ functionality, we designed and synthesized a series of SO$_3$-GQDs with different precursors (named SO$_3$-GQDs-x, $x = 1,2,3$) using the hydrothermal treatment similar to the preparation of aforementioned SO$_3$-GQDs. TEM results show that all SO$_3$-GQDs-x samples have a similar lateral size distribution to SO$_3$-GQDs, as well as an intact graphene crystal structure (Fig. S14). XRD analysis reveals a broad (002) peak at around $2\theta = 25.4°$ for all SO$_3$-GQDs-x samples (Fig. S15). As revealed by FTIR spectra, in addition to the -SO$_3$H and -OH bonds at round 900–1200 and 3300–3500 cm^{-1}, the surface of the newly synthesized three SO$_3$-GQDs-x samples also possess NH$_2$ ($\approx$3180 cm^{-1}) functional groups (Fig. S16) originating from their precursors, which is further confirmed by XPS measurements (Fig. S17) [50, 51]. According to the deconvolution results of XPS S 2p spectra, the -SO$_3$H content increases in the order of SO$_3$-GQDs-3 (2.15 at%) < SO$_3$-GQDs-2 (4.10 at%) < SO$_3$-GQDs-1 (4.39 at%) < SO$_3$-GQDs (7.49 at%) (Fig. S17 and Table S2). To modulate the electronic structure of MoS$_2$, these SO$_3$-GQDs-x were introduced into the preparation of MoS$_2$ as a robust regulator (denoted as ALQD-SO$_3$-1, ALQD-SO$_3$-2, and ALQD-SO$_3$-3). TEM images show that all the ALQD-SO$_3$-x have a sheet morphology, similar to the basal morphology of ALQD-SO$_3$ (Fig. S18), while their heights are thickened with decreasing content of -SO$_3$H functional groups, as determined by their AFM images and XPS data (Figs. S19 and S20), demonstrating the thickness engineering of the functional GQDs to 2D nanomaterials. The phase structures of these ALQD-SO$_3$-x do not undergo any transition upon the addition of these GQDs-SO$_3$-x (Figs. S21 and S22), whereas the content of electro-withdrawing -SO$_3$H group of ALQD-SO$_3$-x follows the trend of SO$_3$-GQDs-x (Fig. S20). Notably, the contact angle test also indicates that the hydrophobicity of ALQD-SO$_3$-x strengthen with their decreased -SO$_3$H group concentrations (Fig. S23). Furthermore, their overpotential

at the current density of η10 emerged in a downward trend, which follows the same trend as the -SO$_3$H content (Figs. S19 and S24). Based on the performance trend of the class of ALQD-SO$_3$-x, we conclude that the electro-withdrawing -SO$_3$ functionalized GQDs engineering strategy applies to MoS$_2$ NS catalysts. The stronger the electron-withdrawing capability of the GQDs modulated MoS$_2$ is, the more the HER performance is promoted [52].

3.4 Classification of the Functional Groups of GQDs on 2H-MoS$_2$

To further verify the effectiveness of electron-withdrawing group functionalized GQDs on MoS$_2$ for HER applications, we synthesized electron-withdrawing -COOH group functionalized GQDs (COOH-GQDs) and electron-donating -OH group functionalized GQDs (OH-GQDs) using a redox method described in our previously reported work [20, 53]. The OH-GQDs and COOH-GQDs manifest a similar lateral size distribution to the aforementioned GQDs (Fig. S25), as well as the intact graphene crystal structure (Fig. S26). XPS analysis confirms the difference in functional groups between the two GQDs (Fig. S27 and Table S3), with the COOH-GQDs exhibiting a significantly higher content of C=O than C-O, while the opposite is true for the OH-GQDs, consistent with the chemical bonding characteristics of -COOH and -OH [54, 55].

Structural characterization and property measurement have been performed to study the corresponding products, i.e., ALQD-COOH and ALQD-OH. The thicknesses of the as-synthesized ALQD-COOH and ALQD-OH are about 10 and 40 nm, respectively (Fig. 4a, b), which agrees with the above-mentioned finding that the electron-withdrawing group functionalized GQDs induce the *in-situ* growth of thinner MoS$_2$ NSs. TEM images (Fig. 4c, d) further confirm their sheet structure characteristics, with the ALQD-COOH displaying fewer-layer NSs and observable COOH-GQDs on its surface [56], while the ALQD-OH shows severe aggregation of NSs, consistent with their AFM data. High resolution TEM images (Fig. 4e, f) further reveal the presence of GQDs on NSs, and XRD pattern (Fig. S28) indicates that the peaks of ALQD-OH roughly match the standard pattern of 2H-MoS$_2$. The strongest diffraction peak of ALQD-COOH is shifted to a lower degree than that of ALQD-OH, in accordance with the trend observed in ALQD-SO$_3$. The
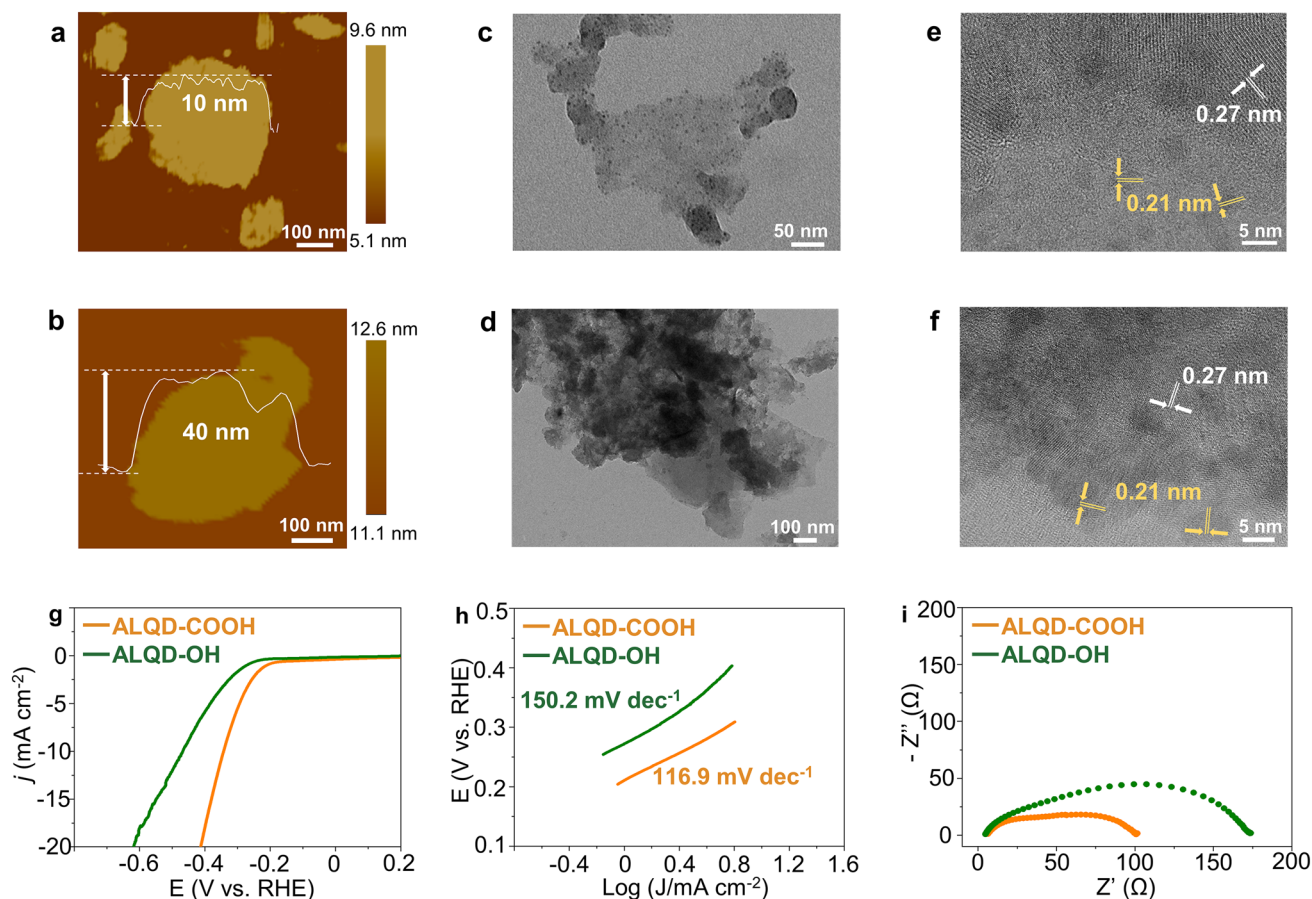
Fig. 4 Morphological characterization and HER performance of ALQD-COOH and ALQD-OH. AFM images of **a** ALQD-COOH and **b** ALQD-OH. TEM images of **c** ALQD-COOH and **d** ALQD-OH. High-resolution TEM images of **e** ALQD-COOH and **f** ALQD-OH. **g** LSV curves of ALQD-COOH and ALQD-OH were performed in 0.5 M H_2SO_4 electrolyte. **h** The corresponding Tafel slopes were derived from LSV curves. **i** Nyquist plots of ALQD-COOH and ALQD-OH

Raman pattern (Fig. S29) clearly shows characteristic peaks at 376 and 398 cm^{-1} of ALQD-OH and ALQD-COOH, which sustains the 2H phase of $2H-MoS_2$ after the introduction of the functionalized GQDs. The chemical states of as-synthesized materials were identified by XPS (Fig. S30). The binding energy of Mo and S in ALQD-COOH is approximately 0.66 and 0.68 eV lower than that of ALQD-OH, indicating that GQDs-COOH can enhance the electron cloud density around the Mo and S atoms and boost their activities. Importantly, the ALQD-COOH introduced by electron-withdrawing -COOH group functionalized GQDs exhibits favorable hydrophilic properties (Fig. S31), and improves HER electrocatalytic performance.

In addition, we measured and analyzed the HER performance of the two samples. As demonstrated in Fig. 4g–i, the LSV curve illustrate the different in their HER performance,

with overpotential at $\eta10$ being 345 and 468 mV for ALQD-COOH and ALQD-OH, respectively. It is worth noting that the HER activities of ALQD-COOH still exhibit a certain gap with ALQD-SO_3 because of the weaker electron-withdrawing capability of the -COOH group than the $-SO_3$ group. Tafel slope is extracted to investigate the reaction kinetics during HER (Fig. 4h) [57]. The Tafel slope of ALQD-COOH (116.9 mV dec^{-1}) is smaller than that of ALQD-OH (150.2 mV dec^{-1}), indicating that the Volmer-Tafel mechanism is the HER pathway. Furthermore, the better HER performance of ALQD-COOH also originates from the fast charge transfer and transport process, as evidenced by the electrochemical impedance spectra (Fig. 4i). Specifically, ALQD-COOH exhibits the lowest intrinsic resistance, as indicated by the steepest slope in the low-frequency region and the smallest charge transfer resistance indicated

by the smallest semicircle in the high-frequency region [58]. All the above results together demonstrate that GQDs functionalized with electron-withdrawing groups such as $-SO_3$ and -COOH can regulate the interlayer structure of MoS_2 during the *in-situ* synthesis process, resulting in rapid charge transfer and superior HER capacities.

Another control experiment was carried out using the electron-donating NH_2-functionalized GQDs (denoted as NH_2-GQDs) to modify the properties of MoS_2 [59, 60]. The NH_2-GQDs was synthesized by introducing ammonia during the synthesis of SO_3-GQDs (see Methods section for more details). The XPS results confirm that the $-NH_2$ group is successfully decorated onto NH_2-GQDs (4.19 at%) and ALQD-NH_2 (0.66 at%) (Fig. S32). NH_2-GQDs has the same graphene structure (Fig. S33) and comparable lateral size distribution as all the GQDs mentioned above (Fig. S34). The thickness of the fabricated ALQD-NH_2 were measured about 65 nm (Fig. S35), which is high away that of ALQD-SO_3. Similar to the role of electron-donating -OH group on the MoS_2, ALQD-NH_2 does not show any improvement in HER performance (Fig. S36). Based on the above characterization results, it can be concluded that incorporating GQDs functionalized with electron-donating group into MoS_2 is detrimental to the HER performance of MoS_2@GQDs catalysts.

4 Conclusions

In summary, we firstly used theoretical calculation to predict the possible formation mechanism of 2H-MoS_2 NSs induced by GQDs and the intrinsic mechanism for improving their HER performance. Our findings indicate that electron-withdrawing groups in GQDs can enlarge the layer spacing of 2H-MoS_2, effectively stimulating the formation of the 2D 2H-MoS_2 NSs. Additionally, we identified both Mo and S as potential active sites, activated by the electron-withdrawing groups of ALQD, which maintain a higher charge density of C atoms connected to the functional group, thereby leading to enhanced HER performance. Guided by our theoretical predictions, we successfully synthesized near atom-layer ALQD-SO_3 using a functionalized GQD-induced *in-situ* bottom-up approach. The obtained ALQD-SO_3 exhibited near atom-layer thickness about 2 nm and long-time storage stability. Remarkably, the synthesized near atom-layer ALQD-SO_3 demonstrated significantly improved HER

performance, delivering a low overpotential of 245 mV to reach a current density of 10 mA cm^{-2} and a small Tafel slope of 93.2 mV dec^{-1} with fast reaction kinetics. Furthermore, the superb electrocatalytic stability was achieved at least 160 h without sharp activity decay, which suggested its prospect applications as a high-performance electrocatalyst. We also unraveled the distinct effects of electron-withdrawing group functionalized GQDs and electron-donating group functionalized GQDs on the construction and HER activity of MoS_2 NSs. Specifically, electron-withdrawing group functionalized GQDs facilitate the formation of NS architectures of MoS_2 and HER proceeding, while electron-donating group functionalized GQDs favor the construction of aggregated bulk MoS_2 and lead to sluggish HER kinetics.

Our results suggest that electron-withdrawing group functionalized GQDs play a vital role in regulating the electronic structure and morphology of 2H-MoS_2. It is worth noting that the strength of the electron-withdrawing group on GQDs ($-SO_3$ vs -COOH) affects the thickness and HER catalytic activity of the obtained 2H-MoS_2 NSs. Therefore, it is worthwhile to explore the possible synthesis pathway of stronger electron-withdrawing groups ($-CF_3$, -CN, etc.) functionalized GQDs for fabricating atom-layer 2H-MoS_2 NSs with more robust electrocatalytic capacities in further study. Our approach enlightens the development of related atom-layer semiconductor electrocatalysts, making them easily accessible for further exploration of their exciting physicochemical properties and applications in electrochemical devices and catalysis. Furthermore, our approach can obtain a large amount of near atom-layer semiconductor electrocatalyst nanomaterials with a simple and safe hydrothermal operation in a short time, rendering it suitable for large-scale production with excellent industrialization prospects.

Declarations

References

1. T.F. Jaramillo, K.P. Jørgensen, J. Bonde, J.H. Nielsen, S. Horch et al., Identification of active edge sites for electrochemical H_2 evolution from MoS_2 nanocatalysts. Science **317**, 100 (2007). https://doi.org/10.1126/science.1141483

2. K.C. Knirsch, N.C. Berner, H.C. Nerl, C.S. Cucinotta, Z. Gholamvand et al., Basal-plane functionalization of chemically exfoliated molybdenum disulfide by diazonium salts. ACS Nano **9**, 6018 (2015). https://doi.org/10.1021/acsnano.5b00965

3. Z.Y. Wu, T. Liao, S. Wang, J.A. Mudiyanselage, A.S. Micallef et al., Conversion of catalytically inert 2D bismuth oxide nanosheets for effective electrochemical hydrogen evolution reaction catalysis via oxygen vacancy concentration modulation. Nano-Micro Lett. **14**, 90 (2022). https://doi.org/10.1007/s40820-022-00832-6

4. Y. An, A. Kuc, P. Petkov, M. Lozada-Hidalgo, T. Heine, On the chemistry and diffusion of hydrogen in the interstitial space of layered crystals h-BN, MoS_2, and graphite. Small **15**, 1901722 (2019). https://doi.org/10.1002/smll.201901722

5. Y.L. Niu, X. Teng, S.Q. Gong, M.Z. Xu, S.G. Sun et al., Engineering two-phase bifunctional oxygen electrocatalysts with tunable and synergetic components for flexible Zn–air batteries. Nano-Micro Lett. **13**, 126 (2021). https://doi.org/10.1007/s40820-021-00650-2

6. X.Y. Chia, M. Pumera, Characteristics and performance of two-dimensional materials for electrocatalysis. Nat. Catal. **1**, 909 (2018). https://doi.org/10.1038/s41929-018-0181-7

7. M. Fan, L. Cui, X. He, X. Zou, Emerging heterogeneous supports for efficient electrocatalysis. Small Methods **6**, e2200855 (2022). https://doi.org/10.1002/smtd.202200855

8. Q. Fu, J. Han, X. Wang, P. Xu, T. Yao et al., 2D transition metal dichalcogenides: design, modulation, and challenges in electrocatalysis. Adv. Mater. **33**, 07818 (2021). https://doi.org/10.1002/adma.201907818

9. G.F. Qian, J.L. Chen, T.Q. Yu, L. Luo, S.B. Yin, N-doped graphene-decorated NiCo alloy coupled with mesoporous NiCoMoO nano-sheet heterojunction for enhanced water electrolysis activity at high current density. Nano-Micro Lett. **13**, 77 (2021). https://doi.org/10.1007/s40820-021-00607-5

10. Y.J. Yang, Y.H. Yu, J. Li, Q.R. Chen, Y.L. Du et al., Engineering ruthenium-based electrocatalysts for effective hydrogen evolution reaction. Nano-Micro Lett. **13**, 160 (2021). https://doi.org/10.1007/s40820-021-00679-3

11. Y. Cao, Roadmap and direction toward high-performance MoS_2 hydrogen evolution catalysts. ACS Nano **15**, 11014 (2021). https://doi.org/10.1021/acsnano.1c01879

12. X. Zhang, F. Jia, S. Song, Recent advances in structural engineering of molybdenum disulfide for electrocatalytic hydrogen evolution reaction. Chem. Eng. J. **405**, 127013 (2021). https://doi.org/10.1016/j.cej.2020.127013

13. Y.F. Huang, R.J. Nielsen, W.A. Goddard, Reaction mechanism for the hydrogen evolution reaction on the basal plane sulfur vacancy site of MoS_2 using grand canonical potential kinetics. J. Am. Chem. Soc. **140**, 16773 (2018). https://doi.org/10.1021/jacs.8b10016

14. K. Kang, S. Xie, L. Huang, Y. Han, P.Y. Huang et al., High-mobility three-atom-thick semiconducting films with wafer-scale homogeneity. Nature **520**, 656 (2015). https://doi.org/10.1038/nature14417

15. J. Shi, P. Yu, F. Liu, P. He, R. Wang et al., 3R MoS_2 with broken inversion symmetry: a promising ultrathin nonlinear optical device. Adv. Mater. **29**, 1701486 (2017). https://doi.org/10.1002/adma.201701486

16. X.X. Han, X.L. Tong, X.C. Liu, A. Chen, X.D. Wen et al., Hydrogen evolution reaction on hybrid catalysts of vertical MoS_2 nanosheets and hydrogenated graphene. ACS Catal. **8**, 1828 (2018). https://doi.org/10.1021/acscatal.7b03316

17. G.F. Qian, J.L. Chen, T.Q. Yu, J.C. Liu, L. Luo et al., Three-phase heterojunction NiMo-based nano-needle for water splitting at industrial alkaline condition. Nano-Micro Lett. **14**, 20 (2022). https://doi.org/10.1007/s40820-021-00744-x

18. H. Zhang, J.G. Gu, Y.L. Zhang, H.Z. Guo, S.N. Zhang et al., Graphene quantum dots modulate stress granule assembly and prevent abnormal phase transition of fused in sarcoma protein. ACS Nano **17**, 10129–10141 (2023). https://doi.org/10.1002/adma.202209086

19. L. Wang, B. Wu, W. Li, Z. Li, J. Zhan et al., Industrial production of ultra-stable sulfonated graphene quantum dots for golgi apparatus imaging. J. Mater. Chem. B **5**, 5355 (2017). https://doi.org/10.1039/c7tb01348e

20. T. Zhang, W. Li, K. Huang, H. Guo, Z. Li et al., Regulation of functional groups on graphene quantum dots directs selective CO_2 to CH_4 conversion. Nat. Commun. **12**, 5265 (2021). https://doi.org/10.1038/s41467-021-25640-1

21. L. Zhou, H.Z. Guo, Z.M. Wang, L. Wang, Achieving efficient incorporation of electron-withdrawing sites into carbon nitride nanosheets for boosting hydrogen generation. Carbon **213**, 118249 (2023). https://doi.org/10.1016/j.carbon.2023.118249

22. G. Kresse, J. Furthmüller, Efficient iterative schemes for ab initio total-energy calculations using a plane-wave basis

set. Phys. Rev. B. **54**, 11169 (1996). https://doi.org/10.1103/PhysRevB.54.11169

23. J.P. Perdew, K. Burke, M. Ernzerhof, Generalized gradient approximation made simple. Phys. Rev. Lett. **78**, 1396 (1997). https://doi.org/10.1103/PhysRevLett.78.1396

24. S. Grimme, Semiempirical GGA-type density functional constructed with a long-range dispersion correction. J. Comput. Chem. **27**, 1787 (2006). https://doi.org/10.1002/jcc.20495

25. A.A. Peterson, F. Abild-Pedersen, F. Studt, J. Rossmeisl, J.K. Nørskov, How copper catalyzes the electroreduction of carbon dioxide into hydrocarbon fuels. Energy Environ. Sci. **3**, 1311 (2010). https://doi.org/10.1039/C0EE00071J

26. P.P. Ewald, Die berechnung optischer und elektrostatischer gitterpotentiale. Ann. Phys. (1920). https://doi.org/10.1002/andp.19213690304

27. S. Nose, A molecular dynamics method for simulations in the canonical ensemble. Mol. Phys. **100**, 189 (2002). https://doi.org/10.1080/00268970110089117

28. H. Hu, X. Zhang, X. Zhang, L. Wu, V.L. Zhang et al., Probing angle-resolved reflection signatures of intralayer and interlayer excitons in monolayer and bilayer MoS_2. Nano Res. **16**, 7844–7850 (2021). https://doi.org/10.1007/s12274-022-5292-4

29. J. Zhang, W. Li, J. Wang, X. Pu, G. Zhang et al., Engineering p-band center of oxygen boosting h^+ intercalation in δ-MnS_2 for aqueous zinc ion batteries. Angew. Chem. Int. Ed. **62**, e202215654 (2023). https://doi.org/10.1002/anie.202215654

30. X. Hai, W. Zhou, K. Chang, H. Pang, H.M. Liu et al., Engineering the crystallinity of MoS_2 monolayers for highly efficient solar hydrogen production. J. Mater. Chem. A **5**, 8591 (2017). https://doi.org/10.1039/c7ta00953d

31. Z.K. Liu, W.D. Hou, H.Z. Guo, Z.M. Wang, L. Wang et al., Functional group modulation in carbon quantum dots for accelerating photocatalytic CO_2 reduction ACS Appl. Mater. Interfaces **15**, 33868–33877 (2023). https://doi.org/10.1021/acsami.3c05440

32. Y. Katagiri, T. Nakamura, A. Ishii, C. Ohata, M. Hasegawa et al., Gate-tunable atomically thin lateral MoS_2 schottky junction patterned by electron beam. Nano Lett. **16**, 3788 (2016). https://doi.org/10.1021/acs.nanolett.6b01186

33. Y. Sun, Y.P. Zang, W.Z. Tian, X.J. Yu, J.Z. Qi et al., Plasma-induced large-area N, Pt-doping and phase engineering of Mo_S2 nanosheets for alkaline hydrogen evolution. Energy Environ. Sci. **15**, 1201 (2022). https://doi.org/10.1039/d1ee03825g

34. Y. Zhou, J.V. Pondick, J.L. Silva, J.M. Woods, D.J. Hynek et al., Unveiling the interfacial effects for enhanced hydrogen evolution reaction on MoS_2/WTe_2 hybrid structures. Small **15**, 1900078 (2019). https://doi.org/10.1002/smll.201900078

35. Y.F. Yu, G.H. Nam, Q.Y. He, X.J. Wu, K. Zhang et al., High phase-purity 1T'-MoS_2- and 1T'-$MoSe_2$- layered crystals. Nat. Chem. **10**, 638 (2018). https://doi.org/10.1038/s41557-018-0035-6

36. Z.F. Zhu, Y.S. Zou, W.D. Hu, Y.B. Li, Y. Gu et al., Near-infrared plasmonic 2D semimetals for applications in communication and biology. Adv. Funct. Mater. **26**, 1793 (2016). https://doi.org/10.1002/adfm.201504884

37. Y. Kang, S. Najmaei, Z. Liu, Y. Bao, Y. Wang et al., Plasmonic hot electron induced structural phase transition in a MoS_2 monolayer. Adv. Mater. **26**, 6467 (2014). https://doi.org/10.1002/adma.201401802

38. Y. Wang, T. Shi, Q.Y. Fan, Y. Liu, A. Zhang et al., Discovering surface structure and the mechanism of graphene oxide-triggered CeO_2–WO_3/TiO_2 catalysts for no abatement with NH_3. ACS Catal. **12**, 8386 (2022). https://doi.org/10.1021/acscatal.2c01364

39. S.P. Sasikala, Y. Singh, L. Bing, T. Yun, S.H. Koo et al., Longitudinal unzipping of 2D transition metal dichalcogenides. Nat. Commun. **11**, 5032 (2020). https://doi.org/10.1038/s41467-020-18810-0

40. H. Liu, Y. Zhao, Y.D. Liu, T.T. Liang, Y.H. Tian et al., Macroporous SnO_2/MoS_2 inverse opal hierarchitecture for highly efficient trace NO_2 gas sensing. Chem. Commun. **59**, 2931 (2023). https://doi.org/10.1039/d2cc06656d

41. X. Wang, Y.W. Zhang, H.N. Si, Q.H. Zhang, J. Wu et al., Single-atom vacancy defect to trigger high-efficiency hydrogen evolution of MoS_2. J. Am. Chem. Soc. **142**, 4298 (2020). https://doi.org/10.1021/jacs.9b12113

42. W.F. Zhai, Y. Chen, Y.D. Liu, T. Sakthivel, Y.Y. Ma et al., Bimetal-incorporated black phosphorene with surface electron deficiency for efficient anti-reconstruction water electrolysis. Adv. Funct. Mater. **33**, 2301565 (2023). https://doi.org/10.1002/adfm.202301565

43. F. Guo, Y. Wang, T. Kang, C. Liu, Y. Shen et al., A Li-dual carbon composite as stable anode material for Li batteries. Energy Storage Mater. **15**, 116 (2018). https://doi.org/10.1016/j.ensm.2018.03.018

44. Y. Li, H. Zhang, T. Xu, Z. Lu, X. Wu et al., Under-water super-aerophobic pine-shaped Pt nanoarray electrode for ultrahigh-performance. Adv. Funct. Mater. **25**, 1737 (2015). https://doi.org/10.1002/adfm.201404250

45. H.Z. Guo, X. Zhang, Z.Y. Chen, L. Zhang, L. Wang et al., High-energy short-wave blue light conversion films via carbon quantum dots for preventing retinal photochemical damage. Carbon **199**, 431 (2022). https://doi.org/10.1016/j.carbon.2022.08.003

46. Z.M. Wang, G. Li, W.D. Hou, H.Z. Guo, L. Wang et al., Insights into the use of Te-O pairs as active centers of carbon nanosheets for efficient electrochemical oxygen reduction. ACS Nano **17**, 8671 (2023). https://doi.org/10.1021/acsnano.3c01662

47. X. Ai, X. Zou, H. Chen, Y. Su, X. Feng et al., Transition-metal-boron intermetallics with strong interatomic d-sp orbital hybridization for high-performance electrocatalysis. Angew. Chem. Int. Ed. **59**, 3961 (2020). https://doi.org/10.1002/anie.201915663

48. Y.D. Liu, T. Sakthivel, F. Hu, Y.H. Tian, D.S. Wu et al., Enhancing the d/p-band center proximity with amorphous-crystalline interface coupling for boosted pH-robust water electrolysis. Adv. Energy. Mater. **13**, 202203797 (2023). https://doi.org/10.1002/aenm.202203797

49. K. Chen, Z.M. Wang, L. Wang, X.Z. Wu, B.J. Hu et al., Boron nanosheet-supported Rh catalysts for hydrogen evolution: a new territory for the strong metal-support interaction effect. Nano-Micro Lett. **13**, 138 (2021). https://doi.org/10.1007/s40820-021-00662-y

50. C. Wu, S. Ding, D. Liu, D. Li, S. Chen et al., A unique Ru-N_4-P coordinated structure synergistically waking up the nonmetal p active site for hydrogen production. AAAS Res. (2020). https://doi.org/10.34133/2020/5860712

51. J. Liu, T. Kong, H.M. Xiong, Mulberry-leaves-derived red-emissive carbon dots for feeding silkworms to produce brightly fluorescent silk. Adv. Mater. **34**, e2200152 (2022). https://doi.org/10.1002/adma.202200152

52. Q. He, D. Tian, H. Jiang, D. Cao, S. Wei et al., Achieving efficient alkaline hydrogen evolution reaction over a Ni_5P_4 catalyst incorporating single-atomic Ru sites. Adv. Mater. **32**, e1906972 (2020). https://doi.org/10.1002/adma.201906972

53. A. Radwan, H.H. Jin, D.P. He, S.C. Mu, Design engineering, synthesis protocols, and energy applications of MOF-Derived electrocatalysts. Nano-Micro Lett. **13**, 132 (2021). https://doi.org/10.1007/s40820-021-00656-w

54. M.M. Fan, Z.M. Wang, K. Sun, A. Wang, Y.Y. Zhao et al., N-B-OH site-activated graphene quantum dots for boosting electrochemical hydrogen peroxide production. Adv. Mater. **35**, 2209086 (2023). https://doi.org/10.1002/adma.22209086

55. X.Y. Shen, Z.M. Wang, H.Z. Guo, Z.D. Lei, Z. Liu et al., Solvent engineering of oxygen-enriched carbon dots for efficient electrochemical hydrogen peroxide production. Small (2023). https://doi.org/10.1002/smll.2303156

56. T.B. Song, Z.H. Huang, X.R. Zhang, J.W. Ni, H.M. Xiong, Nitrogen-doped and sulfonated carbon dots as a multifunctional additive to realize highly reversible aqueous Zinc-ion batteries. Small (2023). https://doi.org/10.1002/smll.202205558

57. G.D. Fu, X.M. Kang, Y. Zhang, X.Q. Yang, L. Wang et al., Coordination effect-promoted durable $Ni(OH)_2$ for energy-saving hydrogen evolution from water/methanol Co-electrocatalysis. Nano-Micro Lett. **14**, 200 (2022). https://doi.org/10.1007/s40820-022-00940-3

58. J. Zhou, J. Lin, H. Sims, C. Jiang, C. Cong et al., Synthesis of Co-doped MoS_2 monolayers with enhanced valley splitting. Adv. Mater. **32**, e1906536 (2020). https://doi.org/10.1002/adma.201906536

59. R.M. Yadav, Z. Li, T. Zhang, O. Sahin, S. Roy et al., Amine-functionalized carbon nanodot electrocatalysts converting carbon dioxide to methane. Adv. Mater. **34**, e2105690 (2022). https://doi.org/10.1002/adma.202105690

60. H.M. Jiang, L.T. Yan, S. Zhang, Y.C. Zhao, X. Yang et al., Electrochemical surface restructuring of phosphorus-doped carbon@MoP electrocatalysts for hydrogen evolution. Nano-Micro Lett. **13**, 215 (2021). https://doi.org/10.1007/s40820-021-00737-w